



ELSEVIER

Comput. Methods Appl. Mech. Engrg. 190 (2001) 6641–6662

**Computer methods
in applied
mechanics and
engineering**

www.elsevier.com/locate/cma

SPH elastic dynamics

J.P. Gray^a, J.J. Monaghan^{a,*}, R.P. Swift^b^a *Epsilon Laboratory, Department of Mathematics and Statistics, Monash University, Clayton 3800, Vic. 3168, Australia*^b *Los Alamos National Laboratory, Los Alamos, NM 87545, USA*

Received 5 July 2000

Abstract

The standard smoothed particle hydrodynamics (SPH) formulation of fluid dynamics can exhibit an instability called the tensile instability. This instability may occur with both positive and negative pressure. Usually the effects are small, but in the case of elastic or brittle solids the effects may be severe. Under tension, a brittle solid can fracture, but it is difficult to disentangle the physical fracture and fragmentation from the nonphysical clumping of SPH particles due to the tensile instability. Recently, one of us (JJM) has shown how this instability can be removed by an artificial stress which introduces negligible errors in long-wavelength modes. In this paper we show how the algorithm can be improved by basing the artificial stress on the signs of the principal stresses. We determine the parameters of the artificial stress from the dispersion relation for elastic waves in a uniform material. We apply the algorithm to oscillating beams, colliding rings and brittle solids. The results are in very good agreement with theory, and with other high-accuracy methods. © 2001 Elsevier Science B.V. All rights reserved.

1. Introduction

Smoothed particle hydrodynamics (SPH) is a gridless Lagrangian particle method which replaces the continuum equations of fluid dynamics by particle equations. The interactions between the particles are determined by interpolation from information at the SPH particles (for references see [11]). When SPH is applied to solids the SPH particles mimic the behaviour of the atoms. If the solid is compressed the atoms repel each other. If it is stretched the atoms attract each other and oppose the stretch. The SPH particles behave the same way except that, when the material is stretched, the attraction can result in the SPH particles forming clumps. This instability was first studied in detail by Sweigle et al. [19], who related it to the sign of the pressure and the sign of the second derivative of the interpolating kernel. It is commonly called the tensile instability.

The instability is also known to occur in gas dynamics where the pressure is positive [20], though detailed studies of SPH for astrophysical gas dynamics using the cubic spline kernel [21] do not show any clumping. A short-wavelength instability identical to the tensile instability was analysed by Philips and Monaghan [15] for the case of magneto-gas dynamics.

There have been a number of attempts to remove this instability by changing the interpolation kernels. Schussler and Schmitt [20] suggested a kernel that gives short-range repulsion for positive pressures. However, their kernel does not have continuous first derivatives and the interpolation is poor. Johnson and Beissel [7] combine normalising the kernels (to reduce boundary errors) with a quadratic kernel which has a nonzero derivative at the origin to reduce the tensile instability. The results are satisfactory; however, the

* Corresponding author. Tel.: +61-3-9905-4431; fax: +61-3-9905-3867.

E-mail addresses: jjm@sapphire.maths.monash.edu.au, joe.monaghan@sci.monash.edu.au (J.J. Monaghan).

second derivative of the kernel is not continuous, and experience shows that smoother kernels (e.g. the cubic spline) give better interpolation when the particles are disordered. Morris [14], in a comprehensive study, examined a variety of interpolation kernels which, while successful in some cases, were not uniformly satisfactory.

In a different approach Randles and Libersky [16] used dissipative terms to remove the instability. However, this appears not to be successful in all cases [9].

SPH can be considered as a simple example of the class of meshless methods (for a review see [1] and for an analysis of the stability see [2]). By making use of one formulation of the meshless methods Dilts [4] generalised SPH by using an interpolant which gives accurate derivatives regardless of the positions of the SPH particles. These more accurate techniques require substantially more work so that even if they eliminate the tensile instability they may not be competitive with other methods. Dilts [4] shows that the tensile instability can be reduced significantly by his method. A promising approach is to use additional points at which the stress is calculated and then mapped to the SPH particles [5]. Recent calculations show that the method leads to a stable algorithm [17].

Because SPH is a particle method it is natural to consider eliminating the tensile instability by mimicking atomic forces rather than changing the interpolation kernel. In a recent paper [12] one of us has shown that the tensile instability in fluids can be removed if a short-range artificial force between particles is introduced. The parameters of the force were chosen to eliminate the tensile instability with minimal errors in the long-wavelength modes. The resulting algorithm is simple, accurate and effective.

This procedure may be generalised to elastic bodies by introducing an artificial stress modelled on the artificial force. Monaghan [12] added an artificial stress to the components of the stress tensor when they were positive (we adopt the usual definition that positive stress denotes tension). This procedure gave good results for the collision of rubber rings [12]. However, whether or not the material is in tension or compression is best determined by working with the principal stresses. The principal stresses can be found for each SPH particle by rotation to the principal axes. The artificial stress should then be added only to those principal stresses which are positive.

We determine the artificial stress in the following way. The form of the artificial stress is similar to that already chosen for an isotropic fluid and involves two parameters. These parameters can be estimated from the dispersion relation for waves propagating in a uniform stressed material. The short-wavelength limit of the dispersion relation shows the tensile instability, and one of the parameters of the artificial stress can be chosen to eliminate the instability. The remaining parameter can be chosen to minimise the errors in the long-wavelength limit.

In this paper we describe how the artificial stress can be calculated, and we give several examples of its application. In particular we show that the SPH algorithm gives good results for large-amplitude elastic vibrations of a rod, the collision of rubber rings and the fracture of metal under tension.

2. The equations for an elastic body

The acceleration equation is

$$\frac{dv^i}{dt} = \frac{1}{\rho} \frac{\partial \sigma^{ij}}{\partial x^j} + g^i, \quad (2.1)$$

where d/dt denotes a derivative following the motion, v^i is the i th component of the velocity, σ^{ij} is the stress tensor, and x^j is the j th cartesian component of the position vector. The stress tensor can be written as

$$\sigma^{ij} = -P\delta^{ij} + S^{ij}, \quad (2.2)$$

where P is the pressure, S^{ij} is the deviatoric stress, and g^i denotes the i th component of a body force per unit mass.

We assume Hooke's law with shear modulus μ . The rate of change of S^{ij} is then given by

$$\frac{dS^{ij}}{dt} = 2\mu \left(\dot{\epsilon}^{ij} - \frac{1}{3} \delta^{ij} \dot{\epsilon}^{kk} \right) + S^{ik} \Omega^{jk} + \Omega^{ik} S^{kj}, \quad (2.3)$$

where

$$\dot{\epsilon}^{ij} = \frac{1}{2} \left(\frac{\partial v^i}{\partial x^j} + \frac{\partial v^j}{\partial x^i} \right), \quad (2.4)$$

and

$$\Omega^{ij} = \frac{1}{2} \left(\frac{\partial v^i}{\partial x^j} - \frac{\partial v^j}{\partial x^i} \right) \quad (2.5)$$

is the rotation tensor. The continuity equation is

$$\frac{d\rho}{dt} = -\rho \nabla \cdot \mathbf{v}. \quad (2.6)$$

We use the following equation of state:

$$P = c_0^2(\rho - \rho_0), \quad (2.7)$$

where ρ_0 is a reference density. The bulk modulus K is $K = \bar{\rho} c_0^2$, and Poisson's ratio ν is given by

$$\nu = \frac{(3K/\mu - 2)}{2(3K/\mu + 2)}. \quad (2.8)$$

3. The SPH equations

The SPH equation for the acceleration of particle a corresponding to (2.1) is

$$\frac{dv_a^i}{dt} = \sum_b m_b \left(\frac{\sigma_a^{ij}}{\rho_a^2} + \frac{\sigma_b^{ij}}{\rho_b^2} + \Pi_{ab} \delta^{ij} \right) \frac{\partial W_{ab}}{\partial x_a^j} + g^i, \quad (3.1)$$

where the summation is over all particles (though in practice only near neighbours contribute because the kernel has finite range), P_b is the pressure, ρ_b is the density, and m_b is the mass of particle b . The term Π_{ab} produces a shear and bulk viscosity (for further details see [11,13]). The kernel W_{ab} is a function of the distance r_{ab} between the particles a and b , and ∇_a denotes the gradient taken with respect to the coordinates of particle a . Because W_{ab} is a function of $|\mathbf{r}_{ab}|$ we can write

$$\nabla_a W_{ab} = \mathbf{r}_{ab} F_{ab}, \quad (3.2)$$

where for vectors we use the notation $\mathbf{r}_{ab} = \mathbf{r}_a - \mathbf{r}_b$. The function $F_{ab} \leq 0$ is an even function of a and b .

In this paper W is the cubic spline kernel normalised for two dimensions [11]. Writing $q = r_{ab}/h$ this kernel has the form:

if $q < 1$ then

$$W(r, h) = \frac{10}{7\pi h^2} \left(1 - \frac{3}{2} q^2 + \frac{3}{4} q^3 \right), \quad (3.3)$$

else, if $1 < q < 2$, then

$$W(r, h) = \frac{5}{14\pi h^2} (2 - q)^3, \quad (3.4)$$

else $W = 0$.

In SPH calculations the particles are usually moved by integrating

$$\frac{d\mathbf{r}_a}{dt} = \mathbf{v}_a; \quad (3.5)$$

however, for problems involving tension it is usually better to use the XSPH alternative [10] where \mathbf{v}_a is replaced by $\hat{\mathbf{v}}_a$, which is defined by

$$\hat{\mathbf{v}}_a = \mathbf{v}_a + \tilde{\epsilon} \sum_b \frac{m_b}{\bar{\rho}_{ab}} (\mathbf{v}_b - \mathbf{v}_a) W_{ab}, \quad (3.6)$$

and $\bar{\rho}_{ab}$ denotes $\frac{1}{2}(\rho_a + \rho_b)$. In this paper we take $\tilde{\epsilon} = 0.5$. The velocity $\hat{\mathbf{v}}_a$ is an average of the particle velocities in the neighbourhood of particle a . The average velocity differs from the actual velocity by terms of order h^2 , which is consistent with the errors in the other SPH equations. It is not necessary to use the same kernel for the velocity averaging as that used for the other equations.

Moving the particles with $\hat{\mathbf{v}}$ does not affect the conservation of linear and angular momentum. It can be seen from (3.6) that reversing the velocity reverses the trajectory in the absence of viscosity in the acceleration equation. Consequently, if we use $\hat{\mathbf{v}}$, we can expect that there is an invariant equivalent to the usual energy. That this is so was established by Holm [6] within the context of the Navier–Stokes alpha turbulence model for incompressible fluids [3,6]. The appropriate invariant for compressible flow is not known.

Moving the particles with $\hat{\mathbf{v}}$ means that advection is defined by

$$\frac{d}{dt} = \frac{\partial}{\partial t} + \hat{\mathbf{v}} \cdot \nabla. \quad (3.7)$$

We calculate the density by solving the continuity equation although, in principle, the density could be calculated by a summation over the particles. For the present calculations, where there is only one material, we use the SPH continuity equation

$$\frac{d\rho_a}{dt} = \sum_b m_b \hat{\mathbf{v}}_{ab} \cdot \nabla_a W_{ab}, \quad (3.8)$$

where the particle velocity has been replaced by $\hat{\mathbf{v}}$ to be consistent with our rule for moving particles. If the calculation involves materials with densities which differ by more than a factor ~ 2 it is preferable to use the alternative equation

$$\frac{d\rho_a}{dt} = \rho_a \sum_b \frac{m_b}{\rho_b} \hat{\mathbf{v}}_{ab} \cdot \nabla_a W_{ab}. \quad (3.9)$$

The rate of change of S^{ij} also depends on the relative motion of the particles which is determined by $\hat{\mathbf{v}}$. Accordingly, for consistency, ϵ^{ij} and Ω^{ij} must be calculated using $\hat{\mathbf{v}}$ instead of \mathbf{v} . Using SPH interpolation the gradients of the velocity can be written as

$$\left(\frac{\partial \hat{v}^j}{\partial x^i} \right)_a = - \sum_b \frac{m_b}{\rho_b} (\hat{v}_a^j - \hat{v}_b^j) \frac{\partial W_{ab}}{\partial x_a^i}. \quad (3.10)$$

To remove the tensile instability we replace the terms

$$\frac{\sigma_a^{ij}}{\rho_a^2} + \frac{\sigma_b^{ij}}{\rho_b^2} + \Pi_{ab} \delta^{ij} \quad (3.11)$$

by

$$\frac{\sigma_a^{ij}}{\rho_a^2} + \frac{\sigma_b^{ij}}{\rho_b^2} + \Pi_{ab} \delta^{ij} + R_{ab}^{ij} f^n, \quad (3.12)$$

where f is defined by

$$f_{ab} = \frac{W(r_{ab})}{W(\Delta p)}, \quad (3.13)$$

and Δp is the particle spacing. In SPH calculations the ratio $h/\Delta p$ is assumed to be constant so that $W(\Delta p)$ is constant. In practice, h is determined from the density, and the local particle spacing is an average estimated from h and the assumed constant ratio $h/\Delta p$.

The cubic spline kernel vanishes beyond $2h$, and between h and $2h$ is $\sim(r - 2h)^3$. Accordingly, f is $\sim(r - 2h)^{3n}$ between h and $2h$. Since we find the optimum n is ~ 4 the effect of the artificial stress is confined to nearest neighbours.

We assume

$$R_{ab}^{ij} = R_a^{ij} + R_b^{ij}, \quad (3.14)$$

and we determine the R_a^{ij} and n from the dispersion equations. Note that if $R^{ij} < 0$ the artificial stress has the same sign as a positive pressure term and acts to keep the particles apart.

4. The exact dispersion relation

To compare with the SPH dispersion relation we derive the dispersion relation for waves in an initially uniform, infinite, elastic material with a constant initial stress. We assume the cartesian axes are chosen so that the initial stress is diagonal. We assume the velocity is small and write the variables in the form

$$\begin{aligned} \mathbf{v} &= \mathbf{V} e^{i(\mathbf{k} \cdot \mathbf{r} - \omega t)}, \\ \mathbf{r} &= \bar{\mathbf{r}} + (X, Y) e^{i(\mathbf{k} \cdot \bar{\mathbf{r}} - \omega t)}, \\ \rho &= \bar{\rho} + \delta\rho, \\ \delta\rho &= D e^{i(\mathbf{k} \cdot \bar{\mathbf{r}} - \omega t)}, \\ P &= \bar{P} + c_0^2 \delta\rho, \\ S^{ij} &= \bar{S}^{ij} + T^{ij} e^{i(\mathbf{k} \cdot \bar{\mathbf{r}} - \omega t)}, \end{aligned} \quad (4.1)$$

where the unperturbed quantities are shown by overbars.

Substituting these expressions into the equations of motion, and taking the components of \mathbf{V} to be V_x and V_y , we find

$$\bar{\rho} \omega V_x = k_x (c_0^2 D - T^{xx}) - k_y T^{xy}, \quad (4.2)$$

and

$$\bar{\rho} \omega V_y = k_y (c_0^2 D - T^{yy}) - k_x T^{xy}. \quad (4.3)$$

The continuity equation becomes

$$D = \frac{\rho}{\omega} (\mathbf{k} \cdot \mathbf{V}), \quad (4.4)$$

and from the rate of change of stress we find

$$T^{xx} = -\frac{2\mu}{3\omega} (2k_x V_x - k_y V_y), \quad (4.5)$$

$$T^{yy} = -\frac{2\mu}{3\omega} (2k_y V_y - k_x V_x), \quad (4.6)$$

and

$$T^{xy} = -\frac{\mu}{\omega} (k_x V_y + k_y V_x) + \frac{\zeta}{\omega} (k_y V_x - k_x V_y), \quad (4.7)$$

where

$$\zeta = \frac{1}{2}(\bar{S}^{xx} - \bar{S}^{yy}). \quad (4.8)$$

Substituting for T^{ij} and D in Eqs. (4.2) and (4.3) we find

$$\bar{\rho}\omega^2 V_x = V_x k_x^2 \left(\bar{\rho}c_0^2 + \frac{4}{3}\mu \right) + V_x k_y^2 (\mu - \zeta) + V_y k_x k_y \left(\bar{\rho}c_0^2 + \frac{1}{3}\mu + \zeta \right). \quad (4.9)$$

In the same way the y component of the acceleration equation becomes

$$\bar{\rho}\omega^2 V_y = V_y k_y^2 \left(\bar{\rho}c_0^2 + \frac{4}{3}\mu \right) + V_y k_x^2 (\mu + \zeta) + V_x k_x k_y \left(\bar{\rho}c_0^2 + \frac{1}{3}\mu - \zeta \right). \quad (4.10)$$

The solution of these equations leads to a quartic equation for ω . This can be readily factorised, and we find two modes. One is a longitudinal mode with

$$\omega^2 = k^2 \left(c_0^2 + \frac{4\mu}{3\bar{\rho}} \right), \quad (4.11)$$

and $\mathbf{V} \propto \mathbf{k}$. The other is a nearly transverse mode with

$$\omega^2 = \frac{\mu k^2}{\bar{\rho}} + \frac{(k_x^2 - k_y^2)(\bar{S}^{xx} - \bar{S}^{yy})}{\bar{\rho}}, \quad (4.12)$$

and

$$\frac{V_x}{V_y} = -\frac{k_y(\bar{\rho}c_0^2 + \frac{\mu}{3} + \zeta)}{k_x(\bar{\rho}c_0^2 + \frac{\mu}{3} - \zeta)}. \quad (4.13)$$

If the initial deviatoric stresses are zero this mode is the standard transverse mode.

5. The SPH dispersion relation

We assume the SPH particles are initially placed at the vertices of a regular grid, for example a grid of square cells each of side Δp . The mass of each particle is then $\bar{\rho}(\Delta p)^2$. We denote the initial position of particle a by $\bar{\mathbf{r}}_a$ and write the perturbation to its position in the form

$$\mathbf{r}_a = \bar{\mathbf{r}}_a + (X, Y)\mathbf{e}^{i(\mathbf{k}\cdot\bar{\mathbf{r}}_a - \omega t)}. \quad (5.1)$$

We write the velocity $\hat{\mathbf{v}}_a$ (see (3.6)) in the form

$$\hat{\mathbf{v}}_a = \hat{\mathbf{V}}\mathbf{e}^{i(\mathbf{k}\cdot\bar{\mathbf{r}}_a - \omega t)}, \quad (5.2)$$

and note from (3.6), with ϵ equal to $\frac{1}{2}$, that the relation between \mathbf{V} and $\hat{\mathbf{V}}$ is

$$\hat{\mathbf{V}} = \mathbf{V} \left[1 - \frac{1}{2}(\Delta p)^2 \sum_b (1 - \cos(\mathbf{k} \cdot \mathbf{r}_{ab})) W_{ab} \right]. \quad (5.3)$$

For sufficiently long wavelengths the summation can be replaced by an integral and, in this limit,

$$\hat{\mathbf{V}} = \frac{1}{2}\mathbf{V}(1 + \tilde{W}), \quad (5.4)$$

where \tilde{W} denotes the Fourier transform of W . This expression shows that $\hat{\mathbf{V}}$ introduces additional dispersion coming from the Fourier transform of the kernel. The absence of complex terms shows that it is not dissipative.

All perturbed variables associated with particle a are denoted by a subscript a and they take the same form as those in the continuum case above except that $\mathbf{k} \cdot \mathbf{r}$ is replaced by $\mathbf{k} \cdot \bar{\mathbf{r}}_a$.

It is convenient to begin with the standard SPH equations and include the artificial stress terms later. Substituting the perturbation variables into the equations of motion, and defining

$$\begin{aligned} \mathbf{A} &= (\Delta p)^2 \sum_b \sin(\mathbf{k} \cdot \mathbf{r}_{ab}) \nabla_a W_{ab}, \\ B_x &= (\Delta p)^2 \sum_b (1 - \cos(\mathbf{k} \cdot \mathbf{r}_{ab})) \frac{\partial^2 W_{ab}}{\partial \bar{x}_a^2}, \\ B_y &= (\Delta p)^2 \sum_b (1 - \cos(\mathbf{k} \cdot \mathbf{r}_{ab})) \frac{\partial^2 W_{ab}}{\partial \bar{y}_a^2}, \\ C &= (\Delta p)^2 \sum_b (1 - \cos(\mathbf{k} \cdot \mathbf{r}_{ab})) \frac{\partial^2 W_{ab}}{\partial \bar{x}_a \partial \bar{y}_a}, \\ \beta &= \frac{1}{2} (\Delta p)^2 \sum_b (1 - \cos(\mathbf{k} \cdot \mathbf{r}_{ab})) W_{ab}, \end{aligned} \quad (5.5)$$

the x component of the acceleration equation becomes

$$\omega V_x = -\frac{2(\bar{P} - \bar{S}^{xx} - \bar{\rho}c_0^2)}{\bar{\rho}\omega} (\hat{\mathbf{V}} \cdot \mathbf{A})_x + 2\frac{(\bar{P} - \bar{S}^{xx})}{\bar{\rho}\omega} (B_x \hat{V}_x + C \hat{V}_y) - \frac{(\Delta p)^2}{\bar{\rho}} T^{xx} A_x - \frac{(\Delta p)^2}{\bar{\rho}} T^{xy} A_y. \quad (5.6)$$

The equation for the y component is identical except that x and y are interchanged. Substituting the perturbations into the equations for the rate of change of stress components we find

$$\begin{aligned} T^{xx} &= \frac{2\mu}{3\bar{\omega}} (2\hat{V}_x A_x - \hat{V}_y A_y), \\ T^{yy} &= \frac{2\mu}{3\bar{\omega}} (2\hat{V}_y A_y - \hat{V}_x A_x), \\ T^{xy} &= \frac{\mu}{\bar{\omega}} (\hat{V}_x A_y + \hat{V}_y A_x) - \frac{\zeta}{\bar{\omega}} (\hat{V}_x A_y - \hat{V}_y A_x), \end{aligned} \quad (5.7)$$

where ζ is defined in (4.8). Substituting these expressions into (5.6) and replacing \hat{V} by V according to (5.3), and the definition of β , we find

$$\begin{aligned} \frac{\omega^2 \bar{\rho} V_x}{(1 - \beta)} &= - (2(\bar{P} - \bar{S}^{xx}) - \bar{\rho}c_0^2) A_x (\mathbf{A} \cdot \mathbf{V}) + 2(\bar{P} - \bar{S}^{xx}) (B_x V_x + C V_y) \\ &\quad + \frac{2\mu}{3} (2V_x A_x - V_y A_y) A_x + \mu (V_x A_y + V_y A_x) A_y - \zeta (V_x A_y - V_y A_x) A_y. \end{aligned} \quad (5.8)$$

In the same way the y component of the acceleration equation leads to

$$\begin{aligned} \frac{\omega^2 \bar{\rho} V_y}{(1 - \beta)} &= - (2(\bar{P} - \bar{S}^{yy}) - \bar{\rho}c_0^2) A_y (\mathbf{A} \cdot \mathbf{V}) + 2(\bar{P} - \bar{S}^{yy}) (B_y V_y + C V_x) \\ &\quad + \frac{2\mu}{3} (2V_y A_y - V_x A_x) A_y + \mu (V_x A_y + V_y A_x) A_x - \zeta (V_x A_y - V_y A_x) A_x. \end{aligned} \quad (5.9)$$

5.1. Long wavelengths

For sufficiently long wavelengths we can approximate the summations defining A , B_x , and C by integrals. We find

$$\begin{aligned}
\mathbf{A} &= -\mathbf{k}\tilde{W}, \\
B_x &= k_x^2 \tilde{W}, \\
C &= k_x k_y \tilde{W},
\end{aligned} \tag{5.10}$$

where \tilde{W} is the Fourier transform of W which, in this approximation, can be taken as 1. Correspondingly, we can take β as zero, and (5.8) becomes

$$\bar{\rho}\omega^2 V_x = V_x \left(k_x^2 \left(\bar{\rho}c_0^2 + \frac{4}{3}\mu \right) + k_y^2 (\mu - \zeta) \right) + V_y \left(c_0^2 + \frac{1}{3}\mu + \zeta \right) k_x k_y, \tag{5.11}$$

which agrees with the continuum equation (4.9). Similarly, the long-wavelength approximation of (5.9) is identical to the continuum equation (4.10). These results show that the SPH perturbation equations are correct in the long-wavelength limit, and the dispersion introduced by the SPH formulation can be determined from the Fourier transform of the kernel.

5.2. The artificial stress

In the present case, where the axes have been chosen so that the stress tensor is diagonal, we only need add the term $R_{ab}^{xx} f^n$ to the x component of the acceleration equation and a term $R_{ab}^{yy} f^n$ to the y component. In general, however, there is a term R_{ab}^{xy} after rotating from the local principal axes to the original axes. Since the initial state is uniform we take

$$R_a^{xx} = R_b^{xx} = R^{xx}, \tag{5.12}$$

and R_{ab}^{xx} (see (3.14)) then equals $2R^{xx}$ with similar expressions for the R^{yy} component.

The right-hand side of the x component of the SPH acceleration equation now includes a term

$$2\bar{\rho}R^{xx}(Xf_{xx} + Yf_{xy}), \tag{5.13}$$

where

$$\begin{aligned}
f_{xx} &= Z \sum (1 - \cos(\mathbf{k} \cdot \mathbf{r}_a)) \frac{\partial^2 W^{n+1}}{\partial x_a^2}, \\
f_{yy} &= Z \sum (1 - \cos(\mathbf{k} \cdot \mathbf{r}_a)) \frac{\partial^2 W^{n+1}}{\partial y_a^2}, \\
f_{xy} &= Z \sum (1 - \cos(\mathbf{k} \cdot \mathbf{r}_a)) \frac{\partial^2 W^{n+1}}{\partial x_a \partial y_a},
\end{aligned} \tag{5.14}$$

and

$$Z = \frac{(\Delta p)^2}{(n+1)W(\Delta p)^n}. \tag{5.15}$$

In terms of the velocity components (5.13) becomes

$$\frac{2i\bar{\rho}R^{xx}}{\omega} (\hat{V}_x f_{xx} + \hat{V}_y f_{xy}). \tag{5.16}$$

In a similar way we find the y component of the acceleration equation becomes

$$\frac{2i\bar{\rho}R^{yy}}{\omega} (\hat{V}_y f_{yy} + \hat{V}_x f_{xy}). \tag{5.17}$$

We now consider how to choose R^{xx} and R^{xy} to prevent short-wavelength instabilities.

5.3. Short wavelengths

The tensile instability is a short-wavelength instability initially involving the clumping of pairs of particles. The rate of growth depends on the initial configuration of the SPH particles, the kernel, the value of h , and the equation of state (see [14] for the nonelastic case). Since our aim is to provide a guide to the form of the artificial stress, rather than study the dispersion relation in detail, we consider two simple cases. In the first of these the particles are placed on the vertices of a grid of square cells each of side Δp . In the second case the configuration is similar to the first except that every second line of particles in the y direction is shifted by $\Delta p/2$ to form a face-centred lattice. We consider in each case waves propagating along the x -axis with $k_x = \pi/\Delta p$, $k_y = 0$. The dangerous modes are the longitudinal modes with $V_x \neq 0$ and $V_y = 0$ since, if these are unstable, clumping occurs. The transverse modes with $V_x = 0$ and $V_y \neq 0$ are benign because, if they become unstable, they result in lines of particles moving vertically very slowly [14]. In the following we assume $h = \Delta p$ to simplify the calculations though we refer to the results for other values of h . A complete discussion of the dispersion relation is complicated and will be given elsewhere.

5.3.1. Square cells

In this case only neighbours within $2\Delta p$ contribute to the summations and both \mathbf{A} and \mathbf{C} vanish. The equations of motion simplify to

$$\frac{\bar{\rho}\omega^2 V_x}{(1-\beta)} = V_x 2B_x(\bar{P} - \bar{S}^{xx}) - 2V_x R^{xx} \bar{\rho}^2 f_{xx}, \quad (5.18)$$

and

$$\frac{\bar{\rho}\omega^2 V_y}{(1-\beta)} = V_y 2B_y(\bar{P} - \bar{S}^{yy}) - 2V_y R^{yy} \bar{\rho}^2 f_{yy}. \quad (5.19)$$

Eq. (5.18) specifies the longitudinal mode with $V_x \neq 0$ and frequency given by

$$\frac{\bar{\rho}\omega^2}{(1-\beta)} = 2B_x(\bar{P} - \bar{S}^{xx}) - 2R^{xx} \bar{\rho}^2 f_{xx}. \quad (5.20)$$

If h equals Δp we can calculate B_x , f_{xx} and β easily. We find

$$\begin{aligned} B_x &= \frac{30}{7\pi(\Delta p)^2} (2 + (2 - \sqrt{2})(3 - \sqrt{2})), \\ f_{xx} &= \frac{30(3n+2)}{7\pi(\Delta p)^2}, \\ \beta &\sim \frac{10}{7\pi} (1 + (2 - \sqrt{2})^3). \end{aligned} \quad (5.21)$$

Because $B_x > 0$ and $(1-\beta) > 0$ the longitudinal mode is stable if $\sigma^{xx} < 0$ (recall that $\sigma^{xx} = -P + S^{xx}$). Hence, if $\sigma^{xx} < 0$, we can choose $R^{xx} = 0$. If $\sigma^{xx} > 0$, the system is in tension, and the mode is unstable unless we choose

$$R^{xx} < -\frac{B_x |\bar{P} - \bar{S}^{xx}|}{\bar{\rho}^2 f_{xx}}, \quad (5.22)$$

or

$$R^{xx} < -\frac{3}{(3n+2)} \frac{|\bar{P} - \bar{S}^{xx}|}{\bar{\rho}^2}. \quad (5.23)$$

This result agrees in the limit of no deviatoric stress, with the results obtained earlier [12]. If $h/\Delta p$ is increased the values of B_x and f_{xx} decrease. Taking account of the way f_{xx} varies with n it is possible to minimise the error in the long-wavelength dispersion relation due to the artificial stress [12] and we find that

for $1 < h/\Delta p < 1.5$ the optimal choice of n has only a slight dependence on h . A good choice is $n = 4$. The variation of B_x and f_{xx} with $h/\Delta p$ does not change the stability properties, but the coefficient $3/(3n + 2)$ in (5.23) decreases with increasing $h/\Delta p$. For example, when $h/\Delta p = 1.4$, the coefficient is reduced by a factor ~ 2 .

Eq. (5.19) describes the transverse mode with $V_y \neq 0$ and frequency

$$\frac{\bar{\rho}\omega^2}{(1 - \beta)} = 2B_y(\bar{P} - \bar{S}^{yy}) - 2R^{yy}\bar{\rho}^2 f_{yy}. \quad (5.24)$$

If $h = \Delta p$ we find $B_y = -0.096/(\Delta p)^2$, and this mode is unstable when $\sigma^{yy} < 0$ if R^{yy} is zero. This instability, as mentioned above, causes lines of particles to move in the y direction rather than to clump. The effect is generally weak because the particles move slowly to a slightly altered, and more stable, array. Fig. 1 illustrates this change of configuration for a periodic array with positive pressure and zero initial deviatoric stress. The left frame of Fig. 1 shows the initial set-up and the second frame shows the state after 10 000 time steps. In these frames $h = \Delta p$. The third frame shows the final configuration starting as before but with $h = 1.5\Delta p$. The configuration is less regular than with $h = \Delta p$ in agreement with the results from the dispersion relation.

We do not consider values of R^{yy} which could stabilise this mode because it is also possible to have the dangerous longitudinal modes propagating in the y direction with $k_x = 0$ and $k_y = \pi/\Delta p$, and these must be stabilised to prevent clumping. This can be achieved by choosing R^{yy} as for R^{xx} in (5.22) (replacing x by y). It is worth noting that for $1.2 < h/\Delta p < 1.7$, we find $B_y > 0$, and the transverse mode becomes stable for $\sigma^{yy} < 0$.

A more comprehensive study of the dispersion relation will be given elsewhere, but we can conclude that the longitudinal (clumping) modes for the square cell array can be eliminated, but the transverse modes will usually be unstable.

5.3.2. Face-centred cells

As we have seen the artificial stress will stabilise the longitudinal mode and prevent clumping. It will not stabilise the transverse mode which causes adjacent lines of particles to move vertically relative to each other. In an SPH simulation of a gas or liquid this results in the particles moving from the initial square grid array to an array which is roughly every vertical line shifted up half a spacing. A vertically propagating transverse mode causes the horizontal lines of particles to shift but the final configuration is the same as that for the horizontally propagating mode.

We therefore consider particles in an array where each horizontal line has particles spaced by Δp and each line is spaced from the next by Δp and shifted by $0.5\Delta p$ horizontally. As before we examine the short-wavelength mode with k_x equal to $\pi/\Delta p$ and k_y zero.

In this case B_x , B_y , f_{xx} , f_{yy} , and A_x are nonzero, and C and A_y are zero. The dispersion relation for the longitudinal mode now becomes

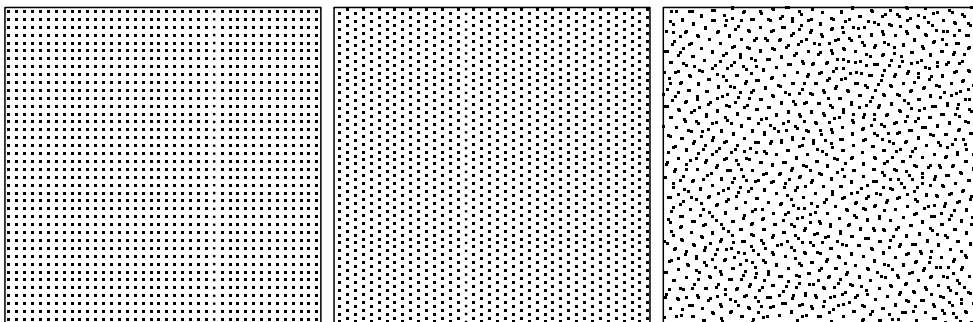


Fig. 1. SPH particle positions for a periodic array with positive pressure. The first frame shows the initial particle positions in the unit cell of the periodic array. The second frame shows the position of the particles after 10 000 steps when h equals Δp . The third frame shows the particle positions after 10 000 steps when h equals $1.5\Delta p$.

$$\frac{\bar{\rho}\omega^2}{(1-\beta)} = 2B_x(\bar{P} - \bar{S}^{xx}) + A_x^2\left(\bar{\rho}c_0^2 + \frac{4}{3}\mu - \bar{P} + \bar{S}^{xx}\right) - 2R^{xx}\bar{\rho}^2f_{xx}. \quad (5.25)$$

If $h = \Delta p$ we find $B_x = 2.81/(\Delta p)^2$, $f_{xx} = 19.7/(\Delta p)^2$ and $A_x = -0.43/\Delta p$. The effect of A_x is therefore slight, but it contributes to stability provided $(\bar{P} - \bar{S}^{xx})$ is sufficiently small compared to $(\bar{\rho}c_0^2 + 4\mu/3)$.

The longitudinal mode is stable for $\sigma^{xx} < 0$. In this case we can take $R^{xx} = 0$. If $\sigma^{xx} > 0$ the mode is stable if

$$R^{xx} < -\frac{2B_x|\bar{P} - \bar{S}^{xx}|}{f_{xx}\bar{\rho}^2}. \quad (5.26)$$

If $h = \Delta p$ we find

$$R^{xx} < -0.14\frac{|\bar{P} - \bar{S}^{xx}|}{\bar{\rho}^2}, \quad (5.27)$$

where the coefficient is smaller than for the previous particle array. As in the case of the square cells we find f_{xx} varies linearly with n . If $h = \Delta p$ we find $f_{xx} \propto (4n + 3.7)$. Making use of this relation, and minimising the error in the long-wavelength modes due to the artificial viscosity [12], we find that the errors are negligible if we choose n equal to 4.

The coefficient (0.14 in (5.27)) decreases with increasing $h/\Delta p$ for $1 < h/\Delta p < 1.5$, which spans the values of h used in practice.

For the transverse mode we find the dispersion relation

$$\frac{\bar{\rho}\omega^2}{(1-\beta)} = 2B_y(\bar{P} - \bar{S}^{yy}) + A_x^2(\mu + \zeta) - 2R^{yy}\bar{\rho}^2f_{yy}. \quad (5.28)$$

If $h = \Delta p$ we find $B_y = 0.52/(\Delta p)^2$ and $f_{yy} = 1.6/(\Delta p)^2$ and, unlike the square cell array, $f_{yy} > 0$ for all values of $h/\Delta p$. If $\sigma^{yy} < 0$ the transverse mode is stable with zero artificial stress (recall that the transverse mode for the square cell configuration was unstable for this case). If $\sigma^{yy} > 0$ then the transverse mode is stable if

$$R^{yy} < -0.32\frac{|\bar{P} - \bar{S}^{yy}|}{\bar{\rho}^2}. \quad (5.29)$$

The coefficient 0.32 is larger than before.

If $h/\Delta p \geq 1.4$ we find that B_y eventually becomes negative. However, the term with A_x^2 now influences the stability significantly. For example, with $h = 1.5\Delta p$, and $(\bar{P} - \bar{S}^{yy}) > 0$, the condition for stability is

$$-0.07(\bar{P} - \bar{S}^{yy}) + 0.18\mu > 0, \quad (5.30)$$

and, because μ is normally greater than $|\bar{P}|$ or $|\bar{S}^{yy}|$, the transverse waves will again be stable. A more comprehensive study of the dispersion relation will be given elsewhere, but we can conclude that the longitudinal (clumping) modes for the face-centred cells can be eliminated in the same way as for the square cells. Unlike the square cell array, the transverse modes for the face-centred array will be stable if $1 < h/\Delta p < 1.4$ and slowly growing if $h/\Delta p > 1.4$.

Although wave propagation is fundamental the conditions determined from the perturbation equations do not necessarily guarantee that, in highly nonlinear problems where the stresses change significantly with position, the SPH algorithm will be stable to clumping. The previous tests [12] of nonlinear problems suggest, however, that the conditions on the artificial stress obtained from the dispersion relation work extremely well.

Accordingly we adopt the following rule for the R^{ij} in the coordinate system where the stress is diagonal:

if $\bar{\sigma}_a^{xx} > 0$ then

$$R_a^{xx} = -\epsilon\frac{\bar{\sigma}_a^{xx}}{\bar{\rho}^2}, \quad (5.31)$$

otherwise R_a^{xx} is zero. The same rule applies for R_a^{yy} with xx replaced by yy . In the calculations we describe here we take $\epsilon \sim 0.3$ and n equal to 4. Under these circumstances the effect of the artificial stress on the long-wavelength modes is negligible. For example, when the stress is due to the pressure alone, the exact long-wavelength dispersion relation $\omega = kc_0$ becomes [12]

$$\omega = kc_0 \left(1 + 0.02 \frac{|\bar{\rho} - \rho_0|}{\rho_0} \right), \quad (5.32)$$

showing that the error term is negligible for the usual variations of density under tension even though the error term does not vanish as the particle spacing decreases.

6. Implementation

6.1. Artificial stress

In the following we confine our analysis to the two-dimensional case and denote the components of the stress tensor using subscripts x and y . The plan is to diagonalise the stress tensor for each particle by rotating the coordinates. We then add an artificial stress term to any of the diagonal components which are positive (i.e. indicating tension). The artificial stress in the original coordinate system is then calculated by rotating the coordinates back. If the angle of rotation for particle a is denoted by θ_a the stress tensor will be diagonal if

$$\tan 2\theta_a = \frac{2\sigma_a^{xy}}{\sigma_a^{xx} - \sigma_a^{yy}}. \quad (6.1)$$

In the rotated frame the new components of the stress tensor for particle a are

$$\bar{\sigma}_a^{xx} = c^2 \sigma_a^{xx} + 2sc \sigma_a^{xy} + s^2 \sigma_a^{yy}, \quad (6.2)$$

and

$$\bar{\sigma}_a^{yy} = s^2 \sigma_a^{xx} + 2sc \sigma_a^{xy} + c^2 \sigma_a^{yy}, \quad (6.3)$$

where c denotes $\cos \theta_a$ and s denotes $\sin \theta_a$. Then \bar{R}^{ij} follows from the rules

if $\bar{\sigma}_a^{xx} > 0$ then

$$\bar{R}_a^{xx} = -\epsilon \frac{\bar{\sigma}_a^{xx}}{\rho^2}, \quad (6.4)$$

otherwise \bar{R}_a^{xx} is zero. The same rule applies for \bar{R}_a^{yy} with xx replaced by yy .

The components of the artificial stress in the original coordinates for particle a are

$$R_a^{xx} = c^2 \bar{R}_a^{xx} + s^2 \bar{R}_a^{yy}, \quad (6.5)$$

$$R_a^{yy} = s^2 \bar{R}_a^{xx} + c^2 \bar{R}_a^{yy}, \quad (6.6)$$

and

$$R_a^{xy} = sc(\bar{R}_a^{xx} - \bar{R}_a^{yy}). \quad (6.7)$$

In the SPH acceleration term involving the interaction between particles a and b , we add to the standard terms

$$\frac{\sigma_a^{ij}}{\rho_a^2} + \frac{\sigma_b^{ij}}{\rho_b^2} + \Pi_{ab} \delta^{ij}, \quad (6.8)$$

the artificial stress terms

$$(R_a^{ij} + R_b^{ij})f^n. \quad (6.9)$$

When calculating the angle θ_a from (6.1) care must be exercised when the denominator becomes very small. If σ^{xx} equals σ^{yy} then we can take θ as $\pi/4$. However, round-off can complicate the calculation. We have found that the results are satisfactory if either double precision is used, or if the denominator is replaced by

$$\sigma^{xx} - \sigma^{yy} + \Delta\sigma, \quad (6.10)$$

where $\Delta\sigma$ has magnitude $10^{-6}\rho_0 c_0^2$, and has the same sign as $(\sigma^{xx} - \sigma^{yy})$.

6.2. Time stepping

We use a predictor-corrector leapfrog for time stepping. To integrate the set of equations describing the change of velocity \mathbf{v} , density ρ and position \mathbf{r} given by

$$\frac{d\mathbf{v}}{dt} = \mathbf{F}, \quad (6.11)$$

$$\frac{d\mathbf{r}}{dt} = \mathbf{v}, \quad (6.12)$$

and

$$\frac{d\rho}{dt} = D, \quad (6.13)$$

we denote the values of the variables at the beginning of a time step by $\mathbf{v}^0, \mathbf{F}^0, \mathbf{r}^0, \rho^0, D^0$ and the time step Δt . The predictor step is

$$\mathbf{v}_p = \mathbf{v}^0 + \Delta t \mathbf{F}^0, \quad (6.14)$$

$$\mathbf{r} = \mathbf{r}^0 + \Delta t \mathbf{v}^0 + \frac{1}{2}(\Delta t)^2 \mathbf{F}^0, \quad (6.15)$$

and

$$\rho_p = \rho^0 + \Delta t D^0. \quad (6.16)$$

The value for \mathbf{r} is not corrected. New values of \mathbf{F} and D are calculated using the predicted quantities, and then corrected values of \mathbf{v} and ρ are calculated according to

$$\mathbf{v} = \mathbf{v}_p + \frac{1}{2} \Delta t (\mathbf{F} - \mathbf{F}^0), \quad (6.17)$$

and

$$\rho = \rho_p + \frac{1}{2} \Delta t (D - D^0). \quad (6.18)$$

For the problems considered here we do not need to include thermal effects. When they are needed the thermal energy equation can be integrated using the same rule as for the density.

7. Test problems

In this section we consider a number of test cases to illustrate the application of the new algorithm. The particles are initially placed on a cartesian grid of square cells since this grid appears to be the most unstable both according to our analysis and the calculations of Swegle [18]. The density is scaled using the reference

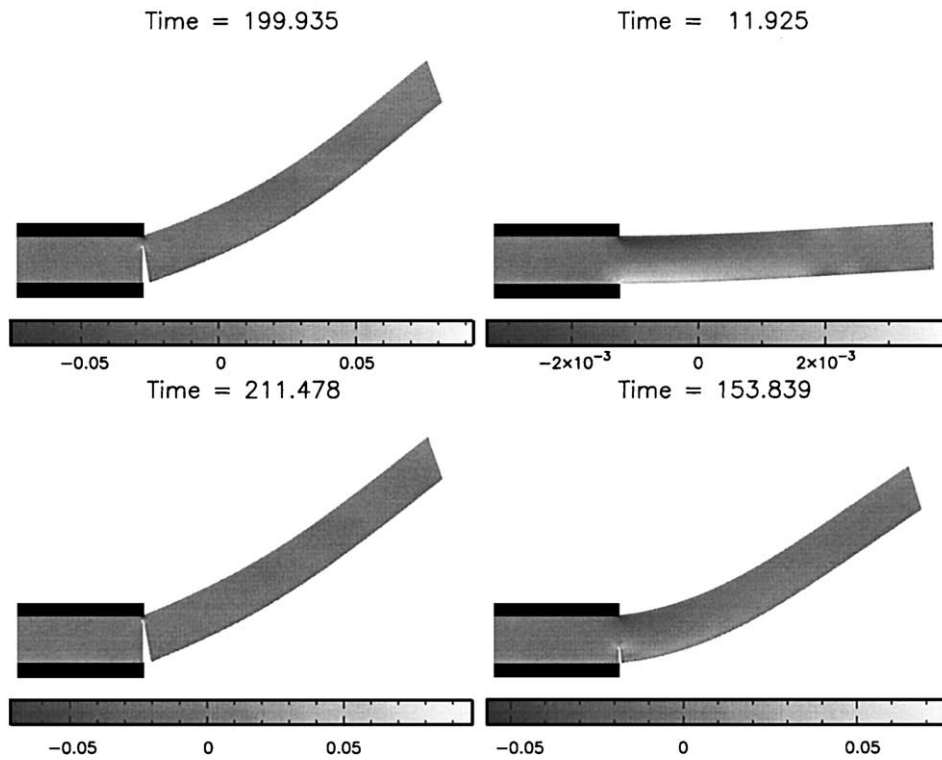


Fig. 2. The oscillation of the plate using the standard SPH algorithm with $\mu = 0.60$ and no artificial stress. Note the fracture which occurs early in the oscillation. Other details are given in the text.

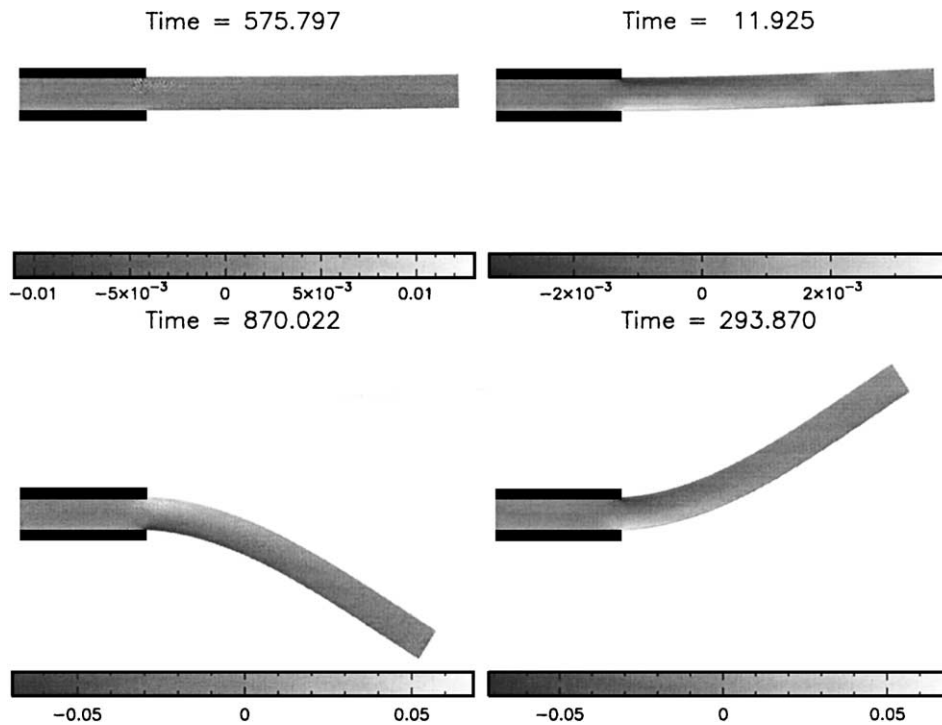


Fig. 3. The oscillation of the plate using the new SPH algorithm with $\mu = 0.60$ and $\epsilon = 0.30$. The oscillation can now be continued for as long as desired.

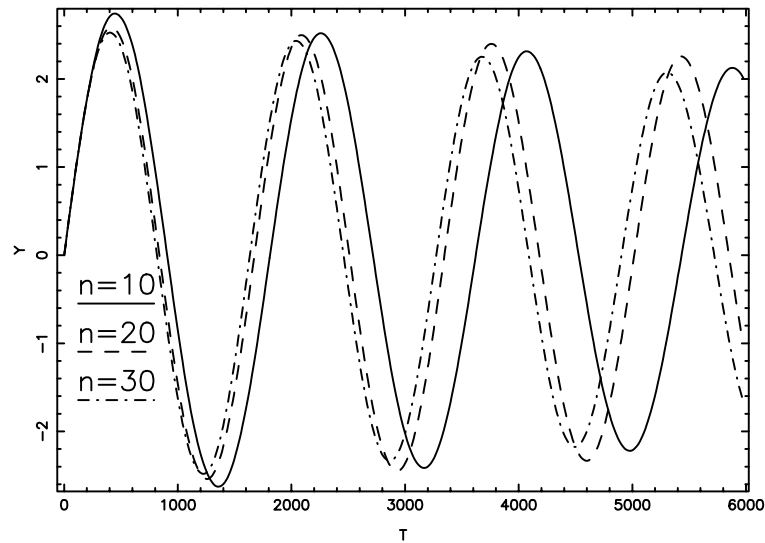


Fig. 4. The vertical position of a point on the end of the plate as a function of time. The graphs are for particle spacings indicated by n the number of particle spacings equivalent to the thickness of the plate $H = 2$ cm. For these oscillations $\mu = 0.22$, $V_f = 0.01$ and $\epsilon = 0.30$.

Table 1

Oscillation periods for a plate with $H = 2$ cm and $L = 20$ cm for various V_f and μ (defined in the text)

V_f	μ	T_{sph}	$T_{\text{theoretical}}$
0.001	0.22	1674.6	1557.0
0.01	0.22	1671.5	1557.0
0.03	0.22	1688.2	1557.0
0.05	0.22	1705.0	1557.0
0.001	0.30	1473.6	1341.9
0.01	0.30	1469.8	1341.9
0.03	0.30	1482.1	1341.9
0.05	0.30	1495.4	1341.9
0.001	0.60	1131.6	1030.4
0.01	0.60	1127.2	1030.4
0.03	0.60	1130.7	1030.4
0.05	0.60	1136.1	1030.4

Table 2

Oscillation periods for a plate with $H = 1$ cm and $L = 20$ cm for various V_f and μ (defined in the text)

V_f	μ	T_{sph}	$T_{\text{theoretical}}$
0.01	0.22	3333.6	3213
0.03	0.22	3385.7	3213
0.05	0.22	3322.8	3213
0.01	0.30	2902.0	2833
0.03	0.30	2977.7	2833
0.05	0.30	2934.9	2833
0.01	0.60	2214.4	2175
0.03	0.60	2221.7	2175
0.05	0.60	2200.4	2175

density, the velocity is scaled using the speed of sound c_0 and the stress terms are scaled in terms of the quantity $\rho_0 c_0^2$. The unit of length is a centimetre. We take $h/(\Delta p)$ to be 1.5.

7.1. Oscillating plate

The theory of a thin oscillating plate with one edge fixed and the other edges free can be found in standard texts [8]. We consider modes which are two-dimensional in a plane perpendicular to the support and the fixed edge. The plate has length L perpendicular to the fixed edge and thickness H . The frequency ω of the oscillation is given by

$$\omega^2 = \frac{EH^2 k^4}{12\rho(1-\nu^2)}, \quad (7.1)$$

where the k is determined by the solutions of

$$\cos(kL) \cosh(kL) = -1. \quad (7.2)$$

For the fundamental mode $kL = 1.875$. For this mode the motion of the plate was initiated with the plate parallel to the x -axis, and with a velocity v_y perpendicular to the plate given by

$$\frac{v_y}{c_0} = V_f \frac{[M(\cos(kx) - \cosh(kx)) - N(\sin(kx) - \sinh(kx))]}{Q}, \quad (7.3)$$

where

$$\begin{aligned} M &= \sin(kL) + \sinh(kL), \\ N &= \cos(kL) + \cosh(kL), \\ Q &= 2(\cos(kL) \sinh(kL) - \sin(kL) \cosh(kL)). \end{aligned} \quad (7.4)$$

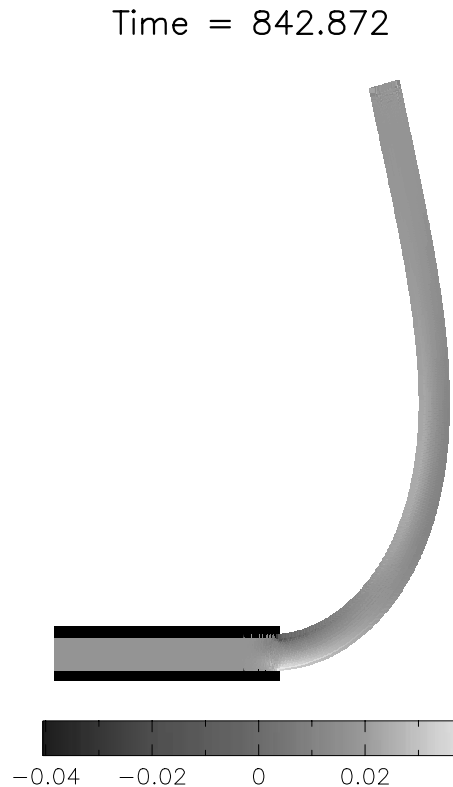


Fig. 5. A highly nonlinear oscillation of a plate with $H = 2$ cm and $L = 20$ cm, with $\mu = 0.22$, $\epsilon = 0.30$, $V_f = 0.05$. This simulation was continued for several oscillations.

The values of V_f , which give the velocity at the free edge of the plate (x equal to L), are given in the tables. The velocity is always much less than the speed of sound.

The plate is clamped between layers of SPH particles which have the same elastic properties as those in the beam but they are not allowed to move. The plate SPH particles between the layers can move, but the motion is always negligible.

The first case we consider uses the standard SPH algorithm with no artificial stress. Fig. 2 shows the motion of the plate for the case where (in our units) μ is 0.60 and V_f is 0.05. The length L is 20 cm and the thickness H is 2 cm. The grey shading scale is proportional to σ^{xx} and is lighter in tension. As expected, the beam breaks where the plate is attached to the support, where the tensile stress is a maximum.

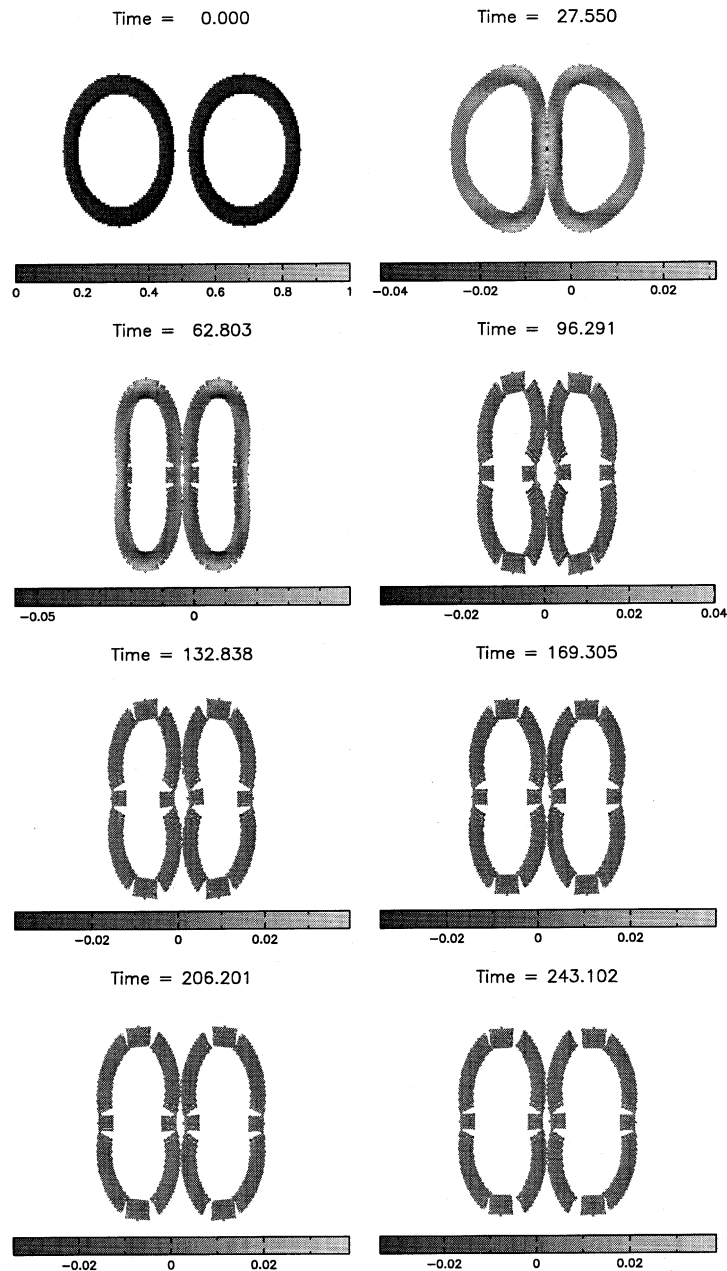


Fig. 6. The collision of two rubber rings using the standard SPH algorithm which produces artificial fracture. Further details are given in the text.

Fig. 3 shows one oscillation of the plate when the artificial stress is included. The beam is now completely stable.

The accuracy can be estimated by comparison with exact results and by studying convergence. Because the theory applies to a very thin plate we expect better agreement with theory as the ratio H/L decreases. We also expect convergence as the resolution improves (i.e. as the particle spacing Δp decreases). In Fig. 4 we show the value of y (the vertical coordinate) for a point at the end of the beam as a function of time and as a function of particle spacing. For this case μ is 0.22 and V_f is 0.01. Although we have not undertaken a complete convergence study, the figure indicates that, as the number of particle spacings across the

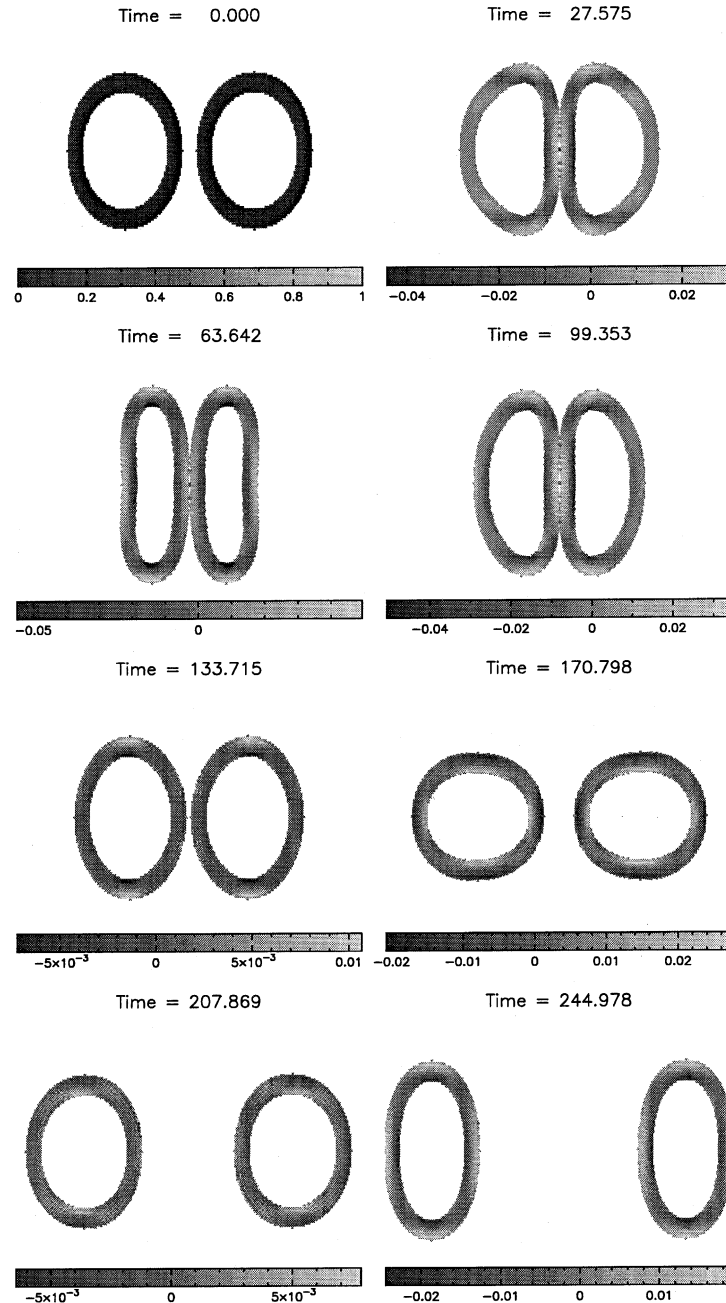


Fig. 7. The collision of two rubber rings using the new SPH algorithm. There is now no fracture. The simulation produces distortion and bounce in good agreement with the TODY code. Further details are given in the text.

thickness n varies from 10 to 20 to 30, the period and amplitude of the oscillations are converging. The amplitude decreases by approximately 6% per oscillation because of dissipation.

Table 1 gives the period T for a wide range of values of μ and V_f . The maximum error between the computed and theoretical results is approximately 10%. However, as mentioned earlier, the theory assumes a plate with negligible H/L . In Table 2 we show results for the case where the length of the plate L is 20 cm and H is 1 cm so that H/L is half its previous value. The agreement is now significantly better, with maximum errors of approximately 3%.

These results show that the SPH code with the new algorithm enables us to simulate elastic motion when the standard algorithm fails. The SPH simulations are in good agreement with theory.

In Fig. 5 we show the particle positions when the amplitude of the oscillation is highly nonlinear. As before the new algorithm simulates the motion with no sign of fracture.

7.2. Colliding rubber rings

Swegle [18] studied the effects of tensile instability by simulating the collision of rubber cylinders. These cylinders should bounce off each other without disintegration. Other codes (see for example [18,22]) simulate the bounce without difficulty, though Sulsky et al. [22] found it necessary to use their second formulation in which the forces were averaged. Swegle [18] found that an SPH simulation of the collision

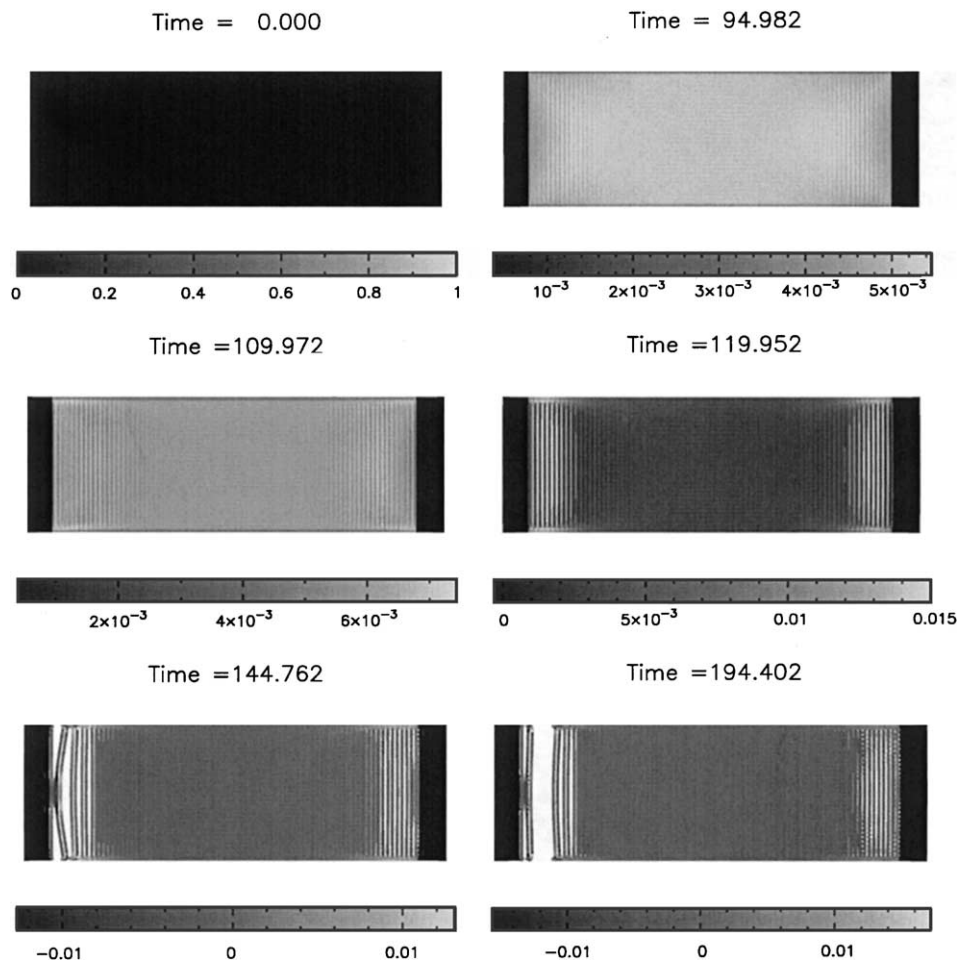


Fig. 8. This figure shows a slab of metal 3 cm long and 1 cm high under tension produced by forcing the particles at each end (shown by the dark band) to accelerate at a fixed rate. The simulation uses the standard SPH algorithm which results in an unphysical fracture near the junction between the particles with forced motion and the other particles. The fracture is evident at a time of 119.

resulted in fragmentation. The fragmentation was greatest when the particles were initially placed on a grid of square cells, and least when they were on a grid cylindrically symmetric about the centre of each cylinder. In the following two-dimensional calculations these cylinders will be referred to as rings.

With our standard scaling μ is 0.22 and the rings are projected with speed 0.059 so the relative speed is 0.118. The rubber rings have inner radius 3 cm and outer radius 4 cm. The particles were initially placed on a grid of square cells since Swegle [18] found this configuration was the most unstable. As a result the rings have a slightly roughened appearance. The initial particle spacing was 0.1 cm.

The positions of the SPH particles are shown in Fig. 6 for the case where the particle spacing is 0.1 cm and ϵ is zero. The rings collide and fracture. In Fig. 7 we show the results with ϵ equal to 0.3. The rings collide, bounce and then oscillate with no fracture. The results differ from those obtained with the TODAY code [18] by between 5% and 10%. Similar results were found with an earlier version of the present algorithm [12].

7.3. Fracture

The final test of the algorithm is to a rectangular slab under tension. The slab is 3 cm long and 1 cm high and the particle spacing is 0.016 cm. The tension is applied by forcing the particles 0.2 cm from each end (shown as the dark band in the figures) to move with a constant acceleration 5×10^{-6} parallel to the long axis of the slab. With this acceleration the ends move a distance $2.5 \times 10^{-6}t^2$ cm in time t . Recall that our unit of time is 1 cm/ c_0 . Accordingly, if t equals 400 the ends will move a distance 0.4 cm, and the strain will be 0.13 in the long-axis direction. Under this strain most materials break.

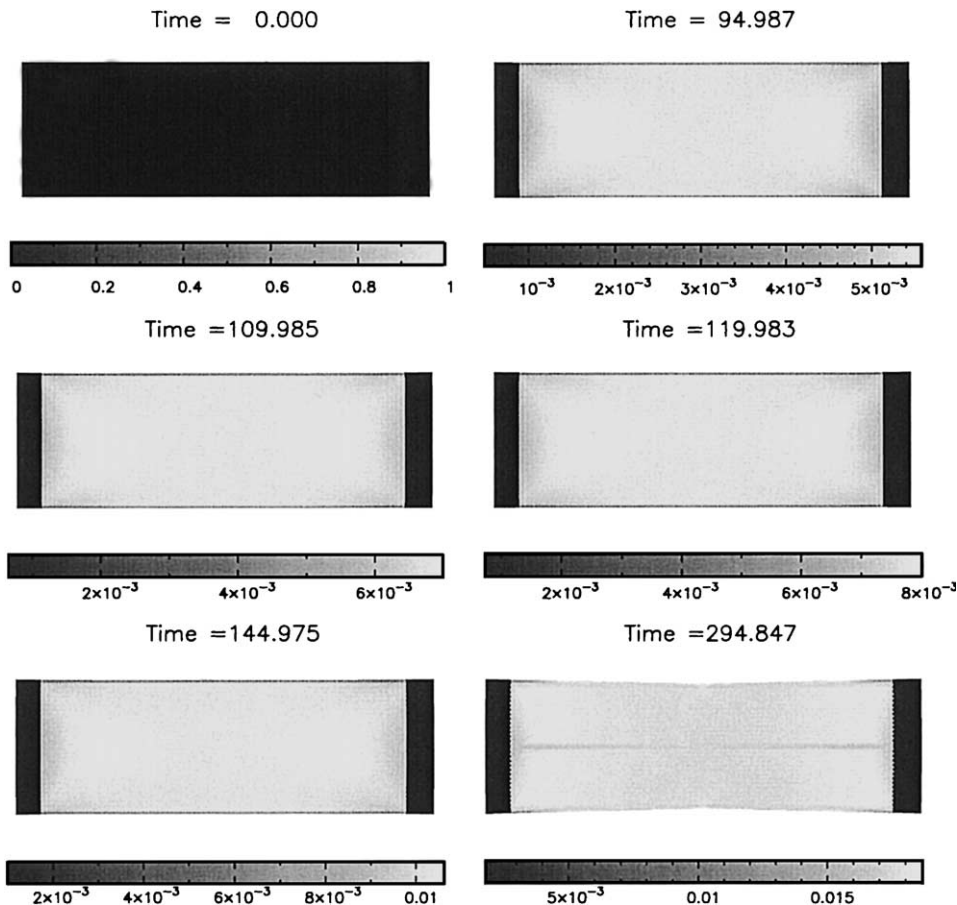


Fig. 9. The same simulation as in Fig. 8 except that the new algorithm was used with $\epsilon = 0.30$. There is now no unphysical fracture.

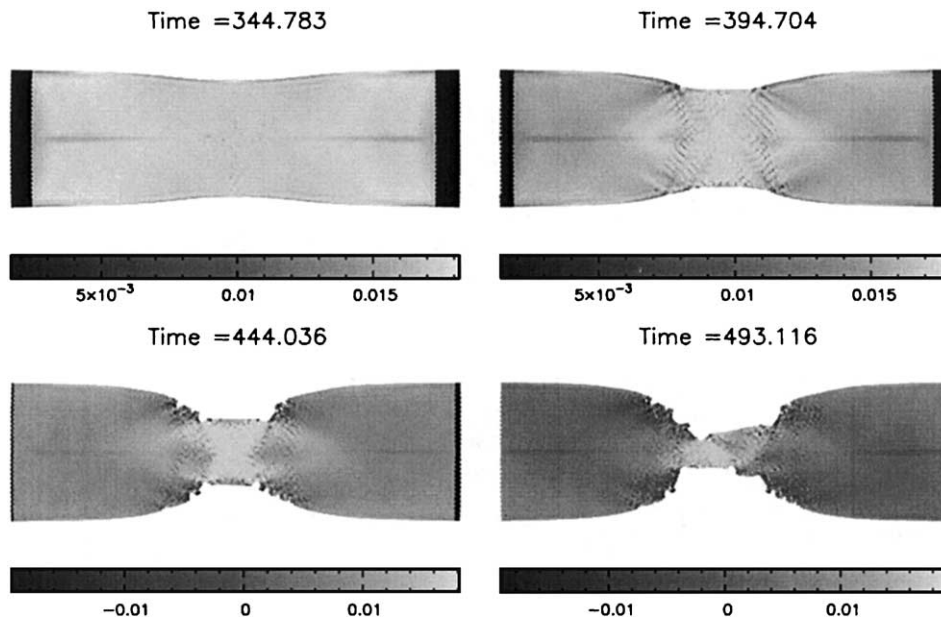


Fig. 10. The simulation of Fig. 9 extended until the strain is approximately 0.13 (at $t = 394$) after which necking occurs.

We take $\mu = 0.3$ in our units and we include plastic behaviour by means of the Von Mises criterion with a yield strength of 0.03. In Fig. 8 we show the results for the standard SPH algorithm. In this case the material fractures unphysically. In Fig. 9 we show the results of the new algorithm with $\epsilon = 0.3$. The elastic material now remains intact (note the times for each frame). If the simulation of Fig. 9 is continued so that the strain exceeds about 0.15, notching occurs, as shown in Fig. 10. Eventually, at $t = 542$, the notching reduces the central neck until it is only ~ 10 particles thick and it fractures. This behaviour is similar to that of real metals.

8. Discussion and conclusions

We can summarise our results as follows:

1. We have analysed the SPH perturbation equations describing wave propagation in a stressed elastic material.
2. The SPH equations agree with the exact equations in the limit of long wavelengths.
3. The dispersion in the long-wavelength limit can be determined from the Fourier transform of the interpolation kernel.
4. The short-wavelength dispersion relation shows that longitudinal modes, which lead to clumping, are unstable under tension but the instability can be removed by a suitable choice of an artificial stress. Whether or not the transverse modes are unstable depends on the particle array. An array of square cells is more unstable than a face-centred array. The transverse modes tend to be benign, that is they grow slowly and move the particles to a more stable configuration. For example, simulations show that, under compression, an array of SPH particles in a square cell array will move to the face-centred array and stabilise if h equals the particle spacing Δp .
5. A simulation of an oscillating plate shows that the new algorithm using the artificial stress is stable and gives good agreement with theory. The standard algorithm results in immediate unphysical fracture.
6. A simulation of colliding rubber rings gives results which agree satisfactorily with other codes.
7. A simulation of a slab of metal under tension shows that the new algorithm behaves similarly to real metals and only fractures when the neck narrows to a thickness equivalent to ~ 10 particle separations. The standard algorithm produces unphysical fracture.

These results show that the new algorithm removes the tensile instability in standard SPH and provides a simple, accurate and robust tool for studies of the dynamics of elastic materials.

References

- [1] T. Belytschko, Y. Krongauz, D. Organ, M. Fleming, P. Krysl, *Comput. Methods Appl. Mech. Engrg.* 139 (1996) 3.
- [2] T. Belytschko, Y. Guo, W.K. Liu, S.P. Xiao, *Int. J. Numer. Meth. Eng.* 48 (2000) 1359.
- [3] S. Chen, D.D. Holm, L.G. Margolin, R. Zhang, *Physica D* 133 (1999) 66.
- [4] G. Dilts, *Int. J. Numer. Meth. Eng.* 44 (1999) 1115.
- [5] C.T. Dyka, P.W. Randles, R.P. Ingel, *Int. J. Numer. Meth. Eng.* 40 (1997) 2325.
- [6] D.D. Holm, *Physica D* 133 (1999) 215.
- [7] G.R. Johnson, S.R. Beissel, *Int. J. Numer. Meth. Eng.* 39 (1997) 2725.
- [8] L.D. Landau, E.M. Lifshitz, *Elasticity, Course of Theoretical Physics*, vol. 7, Pergamon Press, Oxford, 1970.
- [9] D.A. Mandell, C.A. Wingate, L.A. Schwalbe, *Computational brittle fracture using smooth particle hydrodynamics*, Los Alamos National Laboratory Report LA-CP-96-209, 1996.
- [10] J.J. Monaghan, *J. Comput. Phys.* 64 (1989) 2.
- [11] J.J. Monaghan, *Annu. Rev. Astron. Astrophys.* 30 (1992) 543.
- [12] J.J. Monaghan, *SPH without a tensile instability*, *J. Comput. Phys.* (2000).
- [13] J.J. Monaghan, *J. Comput. Phys.* 136 (1997) 298.
- [14] J.P. Morris, *Analysis of SPH with applications*, Ph.D. Thesis, Monash University, Australia, 1996.
- [15] G. Philips, J.J. Monaghan, *Mon. Not. R. Astron. Soc.* 216 (1985) 285.
- [16] P.W. Randles, L.D. Libersky, *Comput. Methods Appl. Mech. Engrg.* 139 (1996) 375.
- [17] P.W. Randles, L.D. Libersky, *Int. J. Numer. Meth. Eng.* 48 (2000) 1445.
- [18] J. Swegle, *SPH in tension*, Memo, Sandia National Laboratories, Albuquerque, USA, 1992.
- [19] J. Swegle, D.L. Hicks, S.W. Attaway, *J. Comput. Phys.* 116 (1995) 123.
- [20] M. Schussler, D. Schmitt, *Astron. Astrophys.* 97 (1981) 373.
- [21] M. Steinmetz, E. Mueller, *Astron. Astrophys.* 268 (1992) 391.
- [22] D. Sulksy, S.-J. Zhou, H.L. Schreyer, *Comput. Phys. Commun.* 87 (1995) 236.